Molecular Insights into Yb(III) Speciation in Sulfate-Bearing Hydrothermal Fluids from X-ray Absorption Spectra Informed by *ab initio* Molecular Dynamics

Xiaodong Zhao,[1,2] Duo Song,[1] Sebastian Mergelsberg,[1] Micah Prange,[1] Daria Boglaienko,[3] Zihua Zhu,[4] Zheming Wang,[1] Carolyn I. Pearce,[3] Chengjun Sun,[5] Kevin M. Rosso,[1] Xiaofeng Guo,[2] Xin Zhang[1 *]

1. Physical & Computational Science Directorate, Pacific Northwest National Laboratory, Richland, Washington 99354, United States
2. Department of Chemistry, Washington State University, Pullman, Washington 99164, United States
3. Energy and Environment Directorate, Pacific Northwest National Laboratory, Richland, Washington 99354, United States
4. Environmental Molecular Sciences Laboratory, Pacific Northwest National Laboratory, Richland, Washington 99354, United States
5. Advanced Photon Source, Argonne National Laboratory, Lemont, Illinois 60439, United States

***Corresponding Authors:** xin.zhang@pnnl.gov (X.Z.)

Abstract

Rare earth elements (REEs) are critical for advanced technologies, yet in hydrothermal aqueous solutions the molecular level details of their interaction with ligands that control their geochemical transport and deposition remain poorly understood. This study elucidates the coordination behavior of Yb^{3+} in sulfate-rich hydrothermal fluids using *in situ* extended X-ray absorption fine structure (EXAFS) spectroscopy and *ab initio* molecular dynamics (AIMD) simulations. By integrating multi-angle EXAFS with AIMD-derived constraints, we precisely resolve Yb^{3+} coordination structures and ligand interactions under hydrothermal conditions. At room temperature, Yb^{3+} is coordinated by five water molecules and two sulfate ligands (coordination number, CN = 8), forming a distorted square antiprism geometry. Increasing temperature induces

progressive dehydration, reducing the hydration shell and favoring stronger sulfate complexation. At 200°C, sulfate ligands reorganize around Yb^{3+}, shifting its geometry to a capped octahedron (CN = 7). At 300°C, sulfate binding dominates, leading to structural reorganization that parallels the onset of sulfate mineral precipitation, consistent with the retrograde solubility of REE sulfates. These findings provide direct molecular-scale evidence that sulfate acts as both a transport and deposition ligand, critically influencing REE mobility in geochemical environments. Our results can also help to refine thermodynamic models of REE speciation in high-temperature hydrothermal fluids and improve our understanding of REE ore formation processes in nature.

Key words: Hydrothermal Fluid, Yb^{3+}, sulfate EXAFS, AIMD, REE Sulfate

1. Introduction:

The demand for rare earth elements (REEs, a group of 17 elements including Sc, Y, and La to Lu) has surged in recent years due to their critical roles in cutting-edge technologies, including renewable energy, electric mobility, and high-strength alloys. This growing industrial dependency has spurred worldwide efforts to identify and exploit alternative geological sources of REEs (Atwood, 2013; Balaram, 2019; Chen et al., 2024; Zhao et al., 2024). Hydrothermal fluids play a crucial role in forming economically significant REE ore deposits, as observed in locations such as the Gallinas Mountains in New Mexico (United States), the Snowbird Deposit in Montana (United States), the Pea Ridge in Missouri (United States), and Bayan Obo in Inner Mongolia (China) (Fan et al., 2016; Harlov et al., 2016; Metz et al., 1985; Smith et al., 2000; Williams-Jones et al., 2000). Over the past two decades, experimental and computational studies have advanced our understanding of REE speciation in hydrothermal systems under elevated temperature and pressure. Techniques such as in situ X-ray absorption spectroscopy (XAS) and *ab initio* molecular

dynamics (AIMD) simulations have been instrumental in elucidating the molecular-level coordination environment of REEs, particularly their interaction with ligands such as chloride, sulfate, and fluoride. Previous studies, including those by Mayanovic *et al.* on REE aqua and chloride complexes (Anderson et al., 2002; Mayanovic et al., 2007, 2009a), which demonstrated the efficacy of *in situ* spectroscopic techniques for characterizing REE hydration and ligand exchange processes. Subsequent studies extended this approach to sulfate and fluoride complexes, highlighting how ligand type, temperature, and pressure affect REE mobility (Guan et al., 2022b; Guan et al., 2020; Louvel et al., 2022b; Migdisov and Williams-Jones, 2008).

Ligands such as Cl^-, CO_3^{2-} and SO_4^{2-} have been considered mainly as transporting ligands in nature, while F^- and PO_4^{3-} have been considered as depositional ligands (Louvel et al., 2022a; Migdisov et al., 2016). Among these, SO_4^{2-} was considered as dominant transporting ligand in many REE deposits, such as Bayan Obo (China) (Lai and Yang, 2013), Maoniuping (China) (Zheng and Liu, 2019) Mountain Pass (United States) depositions (Verplanck et al., 2016) and so on. In hydrothermal fluid, the solubility of REE sulfates undergoes a unique retrograde dissolving behavior: the solubility decreases with increasing temperature, enabling precipitation at elevated temperatures. However, in the presence of prograde soluble alkali sulfates (e.g., Li_2SO_4 and Na_2SO_4) in the hydrothermal fluid (>250°C and 90 MPa), the increased alkali sulfate solubility may enhance the stability of REE sulfate complexes, especially $REE(SO_4)^{2-}$ and $REESO_4^+$(Wan et al., 2023). Furthermore, the recent discovery of liquid–liquid immiscibility (LLI) in REE sulfates revealed the potential for REE^{3+}-SO_4 and REE^{3+}-HSO_4 complexes to become concentrated into a dense liquid phase (DLP) and transport effectively (Wan et al., 2021). These findings underscore the significant role of sulfate in transporting and enriching REEs in hydrothermal environments.

Despite recent advances, the molecular-level structural dynamics of REE sulfates under high-pressure and high-temperature (high P−T) conditions remains poorly understood. A molecular-scale understanding is crucial for understanding and properly interpreting speciation and consequently transport and deposition mechanisms in various hydrothermal environments. Ytterbium (Yb) is selected as the focus of this study because it represents the heavy rare earth element (HREE) group and exhibits a significantly smaller ionic radius compared to previously studied REEs such as La(III), Nd(III), Sm(III) or Er(III) (Migdisov et al., 2006; Migdisov and Williams-Jones, 2008). This allows us to investigate subtle speciation and structural variations driven by lanthanide contraction induced ionic size effects, particularly under high P-T conditions relevant to natural hydrothermal fluids. Furthermore, previous studies on REE–sulfate complexes of Nd(III), Sm(III), and Er(III), have primarily relied on UV-Vis spectroscopy to infer coordination environments (Migdisov et al., 2006; Migdisov and Williams-Jones, 2008). But the UV-Vis lacks the spatial resolution needed to directly determine coordination numbers and bond distances. In contrast, the present study employs synchrotron-based extended X-ray absorption fine structure (EXAFS) spectroscopy, which provides direct, molecular-level insights into the coordination geometry of Yb–SO_4 complexes. But to our knowledge, no prior EXAFS study has specifically examined any Yb–sulfate complexes, despite EXAFS has been widely used to investigate REE aqua, chloride, and carbonate complexes (Guan et al., 2022a; Guan et al., 2020; Louvel et al., 2022a; Migdisov et al., 2019; Migdisov et al., 2016; Migdisov and Williams-Jones, 2008). However, Yb is a strategically critical element due to its widespread applications in modern technologies, including infrared lasers (Takasu et al., 2004), rechargeable batteries (Kim et al., 2021), chemical reducing agents (Girard et al., 1980), and fiber optics (Pask et al., 1995). As such, understanding the speciation and stability of Yb complexes in sulfate-rich environments is not only

of fundamental geochemical interest but also essential for guiding exploration, extraction, and processing strategies for HREE resources.

In hydrothermal fluid, the primary reactions governing REE sulfate complexation in solution are as follows (Migdisov and Williams-Jones, 2008):

$$REE^{3+} + SO_4^{2-} \rightleftharpoons REESO_4^{+} \quad (1)$$

$$REE^{3+} + 2SO_4^{2-} \rightleftharpoons REE(SO_4)_2^{-} \quad (2)$$

$$REESO_4^{+} + SO_4^{2-} \rightleftharpoons REE(SO_4)_2^{-} \quad (3)$$

Key question remains unanswered, which of these reactions is the dominating reaction in HREE sulfate fluid, in other words, it is unclear whether Yb^{3+} preferentially binds mono-sulfate or di-sulfate species. Additionally, how coordination parameters such as bond angles, bond distances, and binding modes vary under high P−T conditions also remains poorly constrained. To address these knowledge gaps, EXAFS spectroscopy coupled with hydrothermal diamond anvil cell (HDAC). However, the integration of HDAC with energy-scanning spectroscopic techniques has long presented challenges, including distortions in XAS spectra caused by Bragg reflections, limited sample thickness, and significant x-ray absorption by the diamond at lower energies (Ingalls et al., 1980b; Ohsumi et al., 1986; Sueno et al., 1986). These issues often lead to overwhelming EXAFS signals into noises and limit the number of EXAFS studies on high P-T hydrothermal fluids. While several artifacts mitigation approaches have been applied, but many of these approaches require specialized equipment (e.g. laser drilled diamonds) (Mayanovic et al., 2007, 2009b; Mayanovic et al., 2002, 2003) or involve hazardous materials (e.g., beryllium gaskets) (Hu et al., 1994; Kaindl et al., 1988). In this study, we adopted a simple multi-angle scanning approach to eliminate Bragg glitches. By rotating the liquid cell up to ±4° relative to the incident beam direction, the Bragg peaks of diamonds in energy space will be shifted, allowing glitch-

containing regions in one scan to be replaced with glitch-free data from another (as illustrated in **Figure. 1**). Besides the diffraction noise issue, the iterative shell-by-shell of EXAFS fitting procedure can be prone to overfitting due to the large number of adjustable parameters, including energy shift (ΔE), change in interatomic distances (ΔR), coordination number (N_i), absorber–back scatterer distance (R_i), and Debye–Waller factor (σ^2), all of which contribute to the normalized EXAFS spectrum as shown in Equation (4):

$$\chi(\mathrm{k}) = \sum_{\mathrm{R}} \frac{S_0^2 CN}{k\mathrm{R}^2} |f(k)| e^{-\frac{2\mathrm{R}}{\lambda(k)}} e^{-2\sigma^2 k^2} \times \sin\left(2k\mathrm{R} + \phi(k)\right) \quad (4)$$

To mitigate this limitation, we integrated AIMD simulations, which provide statistically averaged coordination structures and allow for the generation of theoretical EXAFS spectra (Kerisit and Prange, 2019; Prange et al., 2021). These AIMD-derived spectra are directly compared with experimental data to validate the fitted models, thereby enhancing the reliability and robustness of the structural interpretations. In addition to resolving potential overfitting issues, AIMD offers complementary insights that EXAFS alone cannot provide. These include the denticity of sulfate ligands—allowing for the distinction between mono- and bidentate coordination—along with information on dynamic ligand exchange behavior and qualitative assessments of bonding character, such as π-interactions and partial covalency.

By integrating *in situ* EXAFS measurements with AIMD simulations, this study provides first molecular-level insights into the structural evolution of Yb^{3+} sulfate complexes under hydrothermal conditions. The results reveal thermally induced dehydration, structural reorganization, and systematic changes in how strongly sulfate binds to Yb^{3+} with temperature, adding mechanistic insight into the role of sulfate in REE transport and deposition in geological environments.

2. Material and methods:

2.1. The hydrothermal diamond anvil cell

The HDAC is a versatile instrument designed for high P–T studies of hydrothermal solutions (Bassett et al., 1994). It features two opposing 1/8-carat diamond anvils mounted on tungsten carbide seats, which are affixed to upper and lower stainless-steel platens. These platens are drawn together by three screws and precisely aligned by three guide rods, ensuring stability and reproducibility under extreme P–T conditions. Due to the small sample size and the exceptional thermal conductivity of diamond, temperature gradients within the HDAC are minimal in both vertical and horizontal orientations. As a result, temperature corrections during experiments are typically within ± 5 °C. The HDAC is mounted on a rotation stage, allowing for rotation about two orthogonal axes perpendicular to the incident X-ray beam to optimize experimental geometry. The sample, comprising a fluid phase (solution and vapor bubble), is confined within a chamber created by a 500 μm diameter hole in a 50 μm thick rhenium gasket. The diamond anvils, with 1 mm diameter flat faces, compress the gasket to seal the sample chamber and maintain the desired pressure.

2.2. Sample preparation

Ytterbium(III) sulfate octahydrate ($Yb_2(SO_4)_3 \cdot 8H_2O$, 99.9% purity) was purchased from Thermo Fisher Scientific Inc. (United States). A 0.05 M solution was prepared on-site at the Advanced Photon Source (APS) synchrotron facility by dissolving $Yb_2(SO_4)_3 \cdot 8H_2O$ in deionized water. The solution samples were then loaded into the HDAC chamber using a micropipette under a binocular microscope. While some overflow of the sample solution is often unavoidable during sample loading, it does not affect the X-ray measurements.

2.3. XAS data acquisition and processing

XAS data at the Yb L_3-edge (8944 eV) was collected on the 20-BM-B beamline at APS, Argonne National Laboratory (**Figure 1a**). The measurements were performed in transmission mode, with the incident and transmitted X-ray intensities detected using N_2-gas-filled ionization chambers. To minimize stray radiation around the focused X-ray beam, a pinhole aperture was positioned in front of the incident-beam ionization chamber. The Bragg reflections from diamonds exceed the amplitude of EXAFS oscillations, significantly degrading the quality of the data required for accurate structural analysis (Ingalls et al., 1980a; Ohsumi et al., 1986; Sueno et al., 1986). Various strategies have been proposed to mitigate these artifacts, including measuring multiple spectra at different cell orientations (Freund et al., 1989; Ingalls et al., 1980a; Liu et al., 2020), drilling holes in the diamond for measurements by fluorescence mode (Mayanovic et al., 2007, 2009b; Mayanovic et al., 2002, 2003), using polycrystalline boron carbide (B_4C) anvils (Freund et al., 1989; Sueno et al., 1986), employing low atomic number Beryllium gasket (Hu et al., 1994; Kaindl et al., 1988), and using large-volume multianvil apparatus (Kaindl et al., 1988; Katayama et al., 1997; Liu et al., 2020; Louvel et al., 2022a). In this study, we adopted a practical multi-angle scanning approach to eliminate Bragg glitches and avoided involvement of specialized apparatus and toxic gaskets. At each P–T set, up to eight scans were acquired at different angles up to ±4° relative to the incident beam direction, with each spectrum requiring approximately 30 minutes. As shown in **Figure 1**, in instances where Bragg diffraction peaks were observed, the sample cell was rotated by up to ±4° to shift the diffraction peaks in energy space, and the spectral regions containing Bragg peaks were replaced with corresponding regions devoid of Bragg peaks, ensuring high-quality data for analysis. After Bragg peak removal, the corrected spectra obtained at different detector angles were merged into a single high-quality dataset. This merging process averaged out

angle-dependent variations and reduced noise, resulting in a robust and artifact-free spectrum suitable for *k*-space and *R*-space analysis. To further validate the processed synchrotron data, comparative XAFS measurements were performed using a benchtop X-ray spectrometer. The agreement between the benchtop and synchrotron datasets confirmed the reliability of the processed synchrotron data, enabling its use for detailed structural analysis of the Yb-SO_4 system under high P-T conditions.

In previous studies, DFT-derived geometries were often employed to provide initial guesses for EXAFS shell-by-shell fitting (Xu et al., 2024). This approach improves fitting reliability compared to purely experimental fitting, as DFT-optimized structures generally offer a ground state stable geometry to act as starting point. However, a few DFT-optimized geometry may not necessarily reflect the true structural ensemble present under experimental conditions, especially in dynamic, high-temperature aqueous systems. To address these limitations, a more rigorous and statistically robust approach was adopted in this work. Instead of relying on static DFT-derived geometries, a full ensemble of equilibrium configurations from AIMD trajectories was used to compute theoretical EXAFS spectra (Kerisit et al., 2016; Kerisit et al., 2019; Kerisit and Prange, 2020; Latta et al., 2025; McBriarty et al., 2018). This method captures thermal and structural disorder and provides a direct, unbiased link between simulation and experiments. The theoretical spectra were computed from these trajectories using ab initio multiple scattering calculations and applied a systematic energy shift ($\Delta E = 0–10$ eV) to account for edge alignment uncertainties. The resulting theoretical spectra were then directly compared to the experimental fitted data to assess the degree of agreement. This effectively serves as a sanity check and provides a “double-blind” validation—ensuring that the EXAFS signal could be reproduced by the underlying AIMD ensemble, which

enhances the physical meaning and reliability of the EXAFS interpretation and strengthens confidence in the structural models derived from simulation.

Bench-top EXAFS measurements were collected at room temperature (RT) as a sanity check using an easyXAFS300 instrument (easyXAFS, WA) located at Pacific Northwest National Laboratory (PNNL). The spectra were obtained with a Si(422) spherically bent crystal analyzer and a Mo anode X-ray tube operating at 500 W. Data were corrected for detector deadtime, and the energy was calibrated using a Cr foil standard. Additional spectra were collected with a Ge(422) spherically bent crystal analyzer and a W anode X-ray tube operating at 100 W. Details about these instruments can be found in Seidler *et al.* (Seidler et al., 2014) The data processing and modeling was performed in the Athena and Artemis programs (version 0.9.26).(Ravel and Newville, 2005) The spectra were collected using a Si(551) spherically-bent crystal analyzer and Mo anode x-ray tube operating at 30 kV voltage and 25 mA current. The silicon drift detector deadtime was kept below 30%. The energy calibration of the instrument was done with Cu K-edge (8979 eV). A spectrum collected on a copper foil standard (procured from Exafs materials, CA) was aligned to the one collected at NSLS X11A and retrieved from the Hephaestus database (Ravel and Newville, 2005). Theta-to-energy correction was applied to all the spectra, using theta-to-energy nonlinear shift of the copper standard foil. All the spectra were deadtime corrected. XAS data collection was carried out using an alternating manner between the sample (*It*) and blank (*I0*) to account for possible effects of minor beam instabilities with time. A liquid cell, custom made for the easyXAFS300 instrument, was used for the 0.05 M Yb L_3-edge XANES and EXAFS data collection. A small amount of the sample was injected using a syringe attached to one of the PEEK capillary tubes via a PEEK Lure-Lok adapter while the gas head-space was being released through the other tube. The liquid cell had an aperture of 1 cm, flat and parallel x-ray windows (polyimide

231 or Kapton windows) for uniform pathlength that were sealed by a compression mechanism.
232 Absorption length was controlled by a spacer with a thickness of 1.5 mm. The data processing and
233 modeling was performed in the Athena and Artemis programs (version 0.9.26) (Ravel and
234 Newville, 2005).

235 **2.4. Computational methods**

236 Density functional theory (DFT) (Becke, 2014) and *ab initio* molecular dynamics (AIMD)
237 simulations were performed with the pseudopotential plane-wave NWPW module (Bylaska et al.,
238 2011) implemented in the NWChem software package (Apra et al., 2020; Valiev et al., 2010). The
239 Perdew–Burke–Ernzerhof (PBE) (Perdew et al., 1996) functional was used to account for the
240 exchange correlation energy. Long-range dispersion forces were included in our calculations using
241 the Grimme DFT-D3 method (Grimme et al., 2011). In our plane-wave calculations, the valence
242 electron interactions with the atomic core were approximated with generalized norm-conserving
243 Hamann pseudopotentials (Hamann, 1989) for H, O, and S. These pseudopotentials were
244 constructed using the following core radii: $r_{cs} = r_{cp} = 0.8$ a.u. for H; $r_{cs} = r_{cp} = r_{cd} = 0.7$ a.u. for O;
245 and $r_{cs} = 0.843$ a.u., $r_{cp} = r_{cd} = 0.960$ a.u. for S. Norm-conserving Troullier-Martins
246 pseudopotentials (Troullier and Martins, 1991), which contain 4f, 5s, 5p, 5d, 6s and 6p projectors,
247 were applied for Yb. The following core radii were used to generate these pseudopotentials: r_{cs} =
248 1.618 a.u., $r_{cp} = 1.828$ a.u., $r_{cd} = 1.213$ a.u., and $r_{cf} = 1.403$ a.u.. All the pseudopotentials were
249 modified to the separable form suggested by Kleinman and Bylander (Kleinman and Bylander,
250 1982). Unrestricted calculations were performed since all the systems were open-shell. The
251 electronic wavefunctions were expanded using a plane-wave basis with periodic boundary
252 conditions at the Γ-point with a wavefunction cutoff energy of 544 eV and a density cutoff energy
253 of 1088 eV.

In AIMD, the system was propagated in time using the Car-Parrinello molecular dynamics (CPMD) scheme (Car and Parrinello, 1985). The electronic density is described by Kohn-Sham orbitals within the framework of density functional theory (DFT), and these orbitals are linear combination of a plane-wave basis set. In this work, the simulations were conducted using the canonical ensemble (NVT), with the density of the solution chosen according to the equation of state for NaCl(aq) at similar chloride concentrations and the target temperature and pressure (Driesner, 2007; Driesner and Heinrich, 2007). Each box is cubic in a size by 15Å × 15Å × 15Å, and each box contains one Yb atom, two SO_4 ligands, 113 H_2O molecules, and it was found in sulfate solution of Na_2SO_4 and K_2SO_4 that the density of the sulfate solution changes only very little from RT to 450K (Obšil et al., 1997), hence the box size was not changed during the simulation at different temperatures. The initial box was created by Packmol (Martínez et al., 2009), by placing molecules in defined regions while avoiding atomic overlaps. This ensures a physically reasonable starting configuration, especially for multicomponent or disordered systems like solutions or confined fluids. The generated structure serves as a stable starting point for energy minimization and equilibration in MD simulations. The trajectories of the simulation are shown in Figure S1. Furthermore, in our simulations, we employed a fictitious orbital mass of 600.0 atomic units (au), a standard choice that ensures numerical stability and minimizes artificial energy exchange between the ionic and electronic subsystems. The equations of motion were integrated using the position Verlet algorithm (Verlet, 1967) with a time step of 0.12 fs. All hydrogen atoms were replaced by deuterium to facilitate integration. Temperature control was achieved using the Nosé-Hoover chain thermostat (Blöchl and Parrinello, 1992; Hoover, 1985; Nosé, 1984) for both ions (300 K, 373 K, and 473 K) and electrons (1200 K), and periodic boundary conditions were applied to eliminate surface effects. Each MD simulation was run for 16–30 picoseconds (ps) to

ensure sufficient statistical accuracy. The time-averaged stoichiometric and geometric data were obtained using the Visual Molecular Dynamics (VMD) software (Humphrey et al., 1996). Coordination numbers were derived from the radial distribution functions (RDF), with errors estimated from the differences in RDF integral values at distances of 2.75 Å and 3.25 Å for Yb-O and 2.9 Å and 3.2 Å for Yb-S. The energy and temperature convergency of AIMD results can be found at **Figure S2 - S4**.

3. Results

3.1. Validation of synchrotron EXAFS data

During EXAFS data processing, we employed a spectral correction approach to remove Bragg peaks introduced by the diamond anvils during synchrotron experiments (as described in the methodology section and shown in **Figure 1**). These Bragg peaks could potentially distort the absorption spectra that are critical for EXAFS analysis. To validate our processed synchrotron data, we conducted an RT experiment using the same sample in a liquid cell with a benchtop easyXAFS300 instrument (easyXAFS, WA). Although this liquid cell cannot sustain the high pressures achievable with HDACs, it effectively eliminates Bragg peaks associated with diamond anvils. A comparison of the EXAFS spectra obtained from the synchrotron and the benchtop instrument in k-space (**Figure 1C**) reveals consistent oscillation patterns across the k-range of 2 to 7 $Å^{-1}$, with minimal deviations in amplitude and phase. This consistency indicates that no significant artifacts were introduced during the Bragg peak removal process. Slight variations in intensity at higher *k*-values are likely due to differences in instrumental resolution or noise levels, as the synchrotron provides higher energy resolution compared to the benchtop instrument. Nevertheless, the overall agreement underscores the robustness of the data validation process and

299 confirms that the synchrotron EXAFS spectra can be reliably used for studying the Yb-SO_4 system

300 under high-pressure and high-temperature conditions.

301

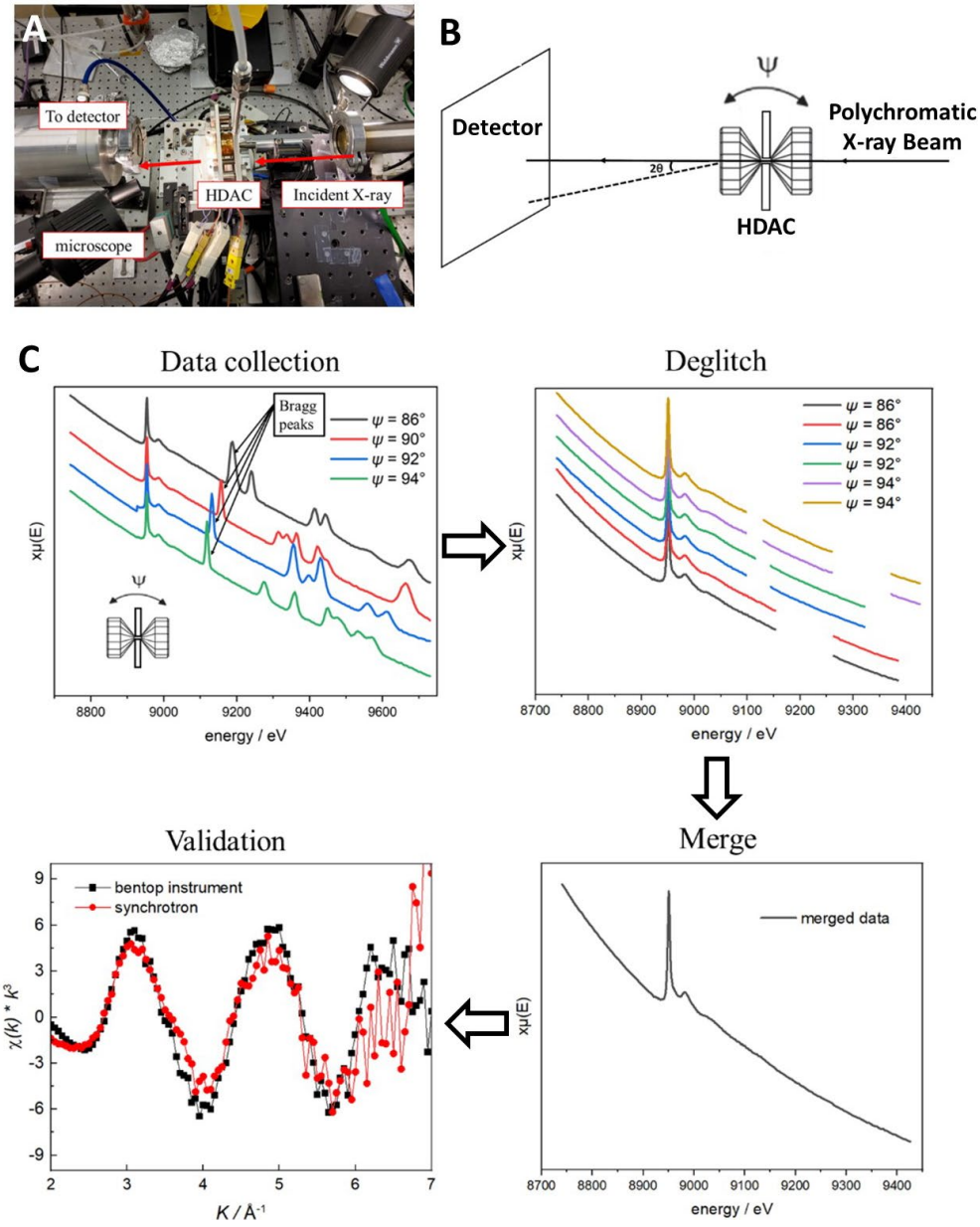

Figure 1. (A) Experimental setup for EXAFS measurements at APS. The HDAC is mounted on a rotation stage. The incident X-ray beam passes through the HDAC and the sample, and the transmitted beam is directed to the detector. A microscope is used for alignment and monitoring the sample within the HDAC. (B) Schematic of the HDAC and its rotation during EXAFS measurements. The detector angle (ψ) varies to minimize artifacts caused by Bragg peaks from

the diamond anvils. (C): Workflow for EXAFS data processing and validation. First step: Raw EXAFS spectra collected at various detector angles at RT (ψ=86° to 94°) showing Bragg peaks caused by diamond anvils. Second step: Corrected spectra after Bragg peak removal, demonstrating clean absorption profiles across the energy range. Third step: Merged EXAFS spectra combining data from multiple angles to reduce noise and ensure spectral consistency. Fourth step: Validation of synchrotron data by comparison with benchtop EXAFS spectra in *k*-space, showing consistent oscillation patterns across the *k*-range (2–7 $Å^{-1}$).

3.2. Local atomic structure and coordination dynamics of Yb^{3+} from experiments

The experimental results from RT to 200°C, fitting and simulated spectra are shown in **Figure 2** and **Figure 3**, and the fitted results are summarized in **Table 1**. At RT, the experimental *k*-space data agreed well with the simulated spectrum. The *R*-space analysis shows distinct peaks, with the first-shell Yb-O peak appearing at ~2.33 Å, corresponding to a coordination number of ~8.4–8.5. Indicated by the AIMD simulation, this shell consists of five water molecules and three sulfate oxygen atoms, with one sulfate ligand exhibited a bidentate mode. The sharpness of the peaks indicates minimal thermal disorder, supported by the low σ^2 value of 0.006 $Å^2$ for the Yb-O shell. The Yb-S peak at ~3.64 Å corresponds to a coordination number of ~2.5, suggesting two sulfate ligand binding with Yb^{3+}. The σ^2 value for Yb-S at RT is also relatively low (0.006–0.014 $Å^2$), highlighting the rigidity of the sulfate coordination shell at ambient conditions.

Table1. Curvefit Parameters for Yb L-III edge EXAFS from RT to 200°C

Temperature	Path	CN #	R/Å	σ^2/ $Å^2$	Temperature	Path	CN #	R/Å	σ^2/ $Å^2$
RT (bench)	Yb-O	8.4	2.33(3)	0.006(1)	100°C	Yb-O	8.5	2.35(1)	0.010(3)
RT (bench)	Yb-S	2.5	3.66(1)	0.006(8)	100°C	Yb-S	2.5	3.68(16)	0.017(31)
RT (synchrotron)	Yb-O	8.5	2.32(1)	0.010(1)	200°C	Yb-O	7.8	2.34(2)	0.017(3)

RT (synchrotron)	Yb-S	2.6	3.64(2)	0.014(9)		200°C	Yb-S	1.7	3.64(1)	0.006(20)

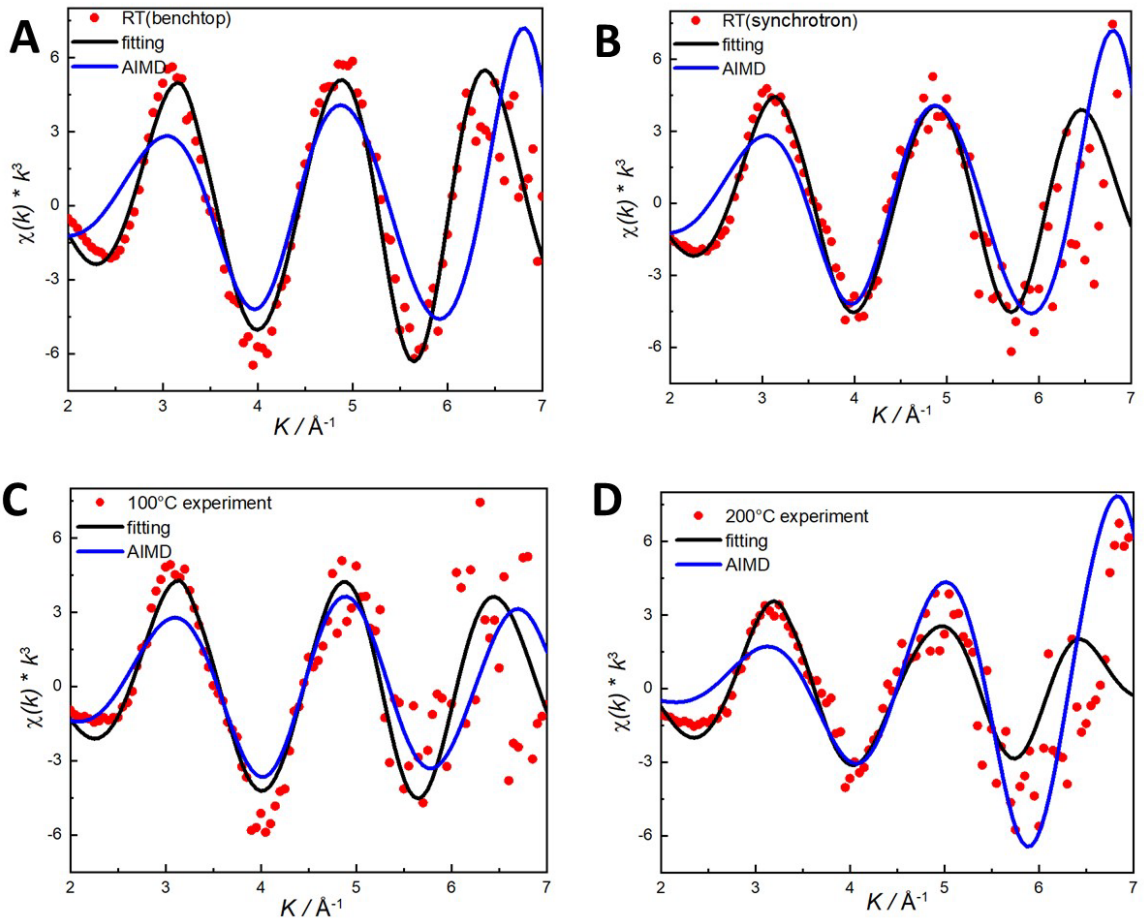

Figure 2. Yb L-III edge EXAFS for 0.05M $Yb_2(SO_4)_3$, shown in k^3-weighted k-space from 2 to 7 $Å^{-1}$. (A) RT data measured with a benchtop instrument (red points), theoretical curve fit (black line), and AIMD simulation (blue line). (B) RT data measured at a synchrotron (red points), theoretical curve fit (black line), and AIMD simulation (blue line). (C) Data collected at 100°C (red points), theoretical curve fit (black line), and AIMD simulation (blue line). (D) Data collected at 200°C (red points), theoretical curve fit (black line), and AIMD simulation (blue line). The consistency across experimental and simulated data highlights the accuracy of the modeling and validation processes.

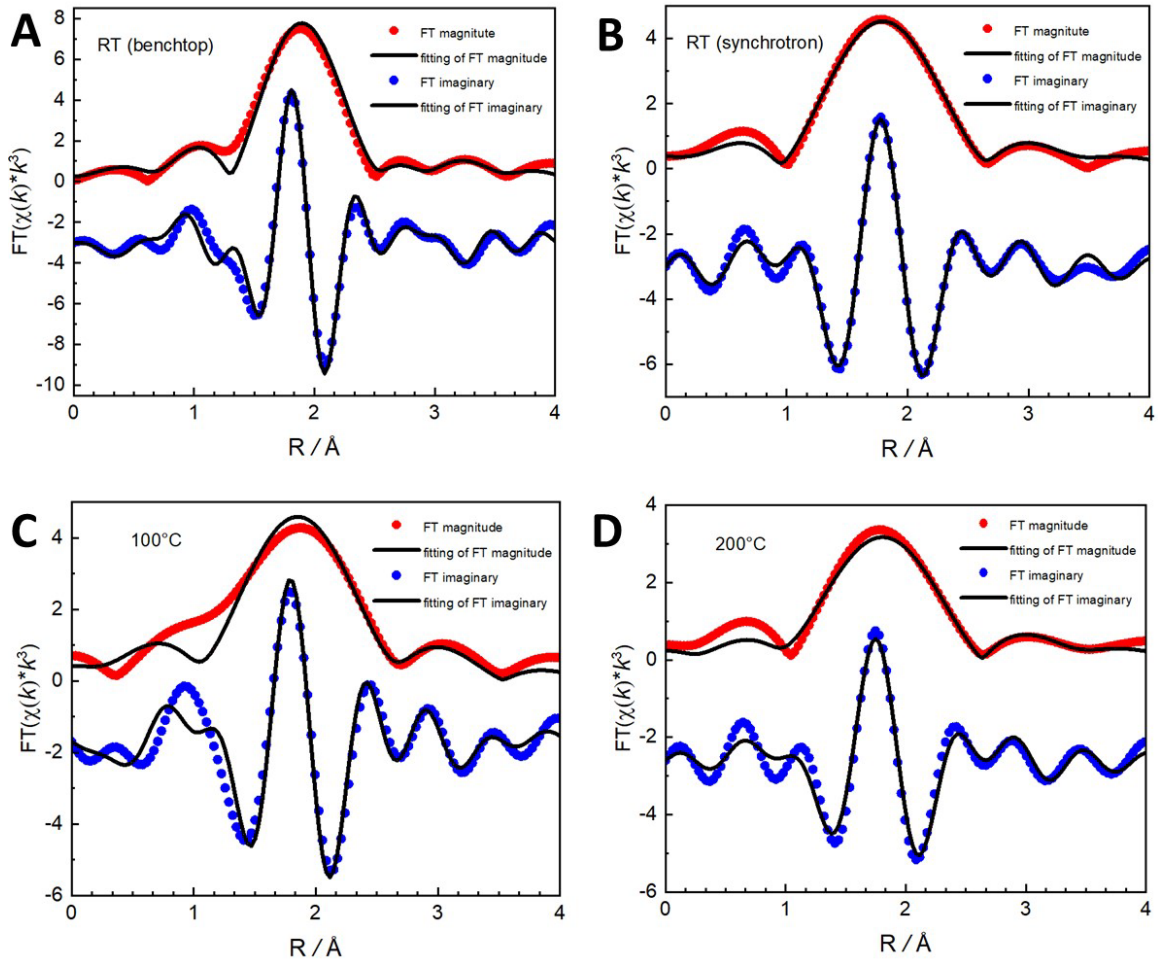

Figure 3. Fourier-transformed Yb L-III edge EXAFS for 0.05M $Yb_2(SO_4)_3$ in *R*-space and not phase-corrected. (A) Data collected at RT using a benchtop instrument: red points represent the Fourier-transformed magnitude, blue points the Fourier-transformed imaginary component, and black lines the curve fits for both. (B) Data collected at RT using a synchrotron instrument with the same labeling scheme. (C) Data collected at 100°C with matching Fourier-transformed components and curve fits. (D) Data collected at 200°C matching Fourier-transformed components and curve fits.

As the temperature increases to 100°C, the first-shell Yb-O peak in *R*-space shifts slightly to ~2.35 Å accompanied by peak broadening and a slight increase in the Debye-Waller factor to 0.010 Å^2. These changes suggest an elongation of Yb–O bonds and increased structural disorder. Despite these changes, the CN remains stable at ~8.5, with Yb^{3+} retaining its hydration shell of five water molecules and sulfate ligands. For Yb-S, the peak shifts slightly to ~3.68 Å, with a CN of ~2.5 and a σ^2 value of 0.017 Å^2. This indicates that sulfate ligands remain bound but exhibit slightly more

flexibility compared to RT. At 200°C, significant structural changes are observed, driven by dehydration and reorganization of the coordination shell. The $\chi(k)*k^3$ oscillations are noticeably broader, reflecting greater thermal disorder. In the *R*-space, the first-shell Yb-O peak shifts further to ~2.34 Å with diminished intensity, indicating a reduction in the number of coordinating oxygen atoms. The CN decreases to ~7.8 with one water molecule removed from the hydration shell suggested by the AIMD simulation. The σ^2 value for the Yb-O shell increases to 0.017 Å^2, implying greater thermal motion and bond variability. Meanwhile, the Yb-S peak becomes less intense, with the CN decreasing to ~1.7 and the σ^2 value dropping to 0.006 Å^2. This suggests that sulfate groups are still coordinating with Yb by a rigid bond, which is potentially due to stronger interactions with the reduced number of sulfate ligands.

Overall, the structural evolution of Yb^{3+} from RT to 200°C reflects the interplay between hydration, sulfate binding, and thermal effects. At RT, the Yb coordination environment is characterized by a dense hydration shell and stable sulfate binding. As the temperature increases to 100°C, the coordination shell remains intact, with only minor elongation of Yb-O bonds and slight increases in disorder. However, at 200°C, the Yb-S bond length (~3.64 Å) remains stable, and the decreased σ^2 value indicates that the remaining sulfate ligands bind more rigidly to Yb^{3+}. The loss of coordinating water molecules reduces competition for coordination sites and enhances electrostatic interactions between Yb^{3+} and the divalent sulfate. Additionally, the bi-dentate binding mode in sulfate can effectively chelate the Yb with a stable and rigid framework. The structural reorganization at high temperatures further favors sulfate ligands occupying optimal positions despite the reduced coordination number. These observations are consistent with the picture that sulfate serves as a transport ligand at high temperature, at least until 200°C.

At 300°C, the EXAFS indicates a distinct precipitation condition for the Yb-SO_4 system. The *k*-space data (**Figure 4A, Table 2**) shows dampened oscillations compared to lower temperatures, indicating greater thermal disorder and possible structural reorganization. The *R*-space data (**Figure 4B, Table 2**) demonstrates broadened peaks, reflecting increased variability in bond lengths and reduced coordination numbers. More importantly, the total CN drops to ~7.2 and the Yb-S CN increases to ~3.5, which suggests dehydration of the complex while yet retaining sulfate ligands. These changes suggest that sulfate ligands bind more strongly with Yb^{3+} as the hydration shell diminishes, likely driving the formation of more ordered sulfate-rich solids, which is consistent with the retrograde solubility behavior of Yb-SO_4 (Cetiner et al., 2005; Cui et al., 2020; Wan et al., 2023). Due to the resolution limitation of the optical scope in the experimental set-up, the exact precipitation temperature could not be determined. Previous solubility data did not cover temperature above 200°C (Judge et al., 2023), hence, we could only conclude that the precipitation temperature is between 200°C and 300°C, further experiments are highly recommended to resolve a precise precipitation temperature. Comparisons to diffraction data for crystalline $Yb_2(SO_4)_3 \cdot 8H_2O$ indicate that the high-temperature coordination environment approaches that of a crystalline solid, where Yb-S bonds are dominant (CN ~4, bond length ~3.60 Å). The reduced CN for Yb-O at 300°C and the dominance of Yb-S coordination suggests the formation of a partially dehydrated crystal.

Table 2. Curvefit Parameters for Yb L-III edge EXAFS at 300°C and bond lengths from diffraction data of $Yb_2(SO_4)_3 \cdot 8H_2O$ solid at RT.

system	Path	CN #	R/Å	σ^2/ Å^2
HDAC (300°C)	Yb-O	7.2	2.33(8)	0.012(1)
HDAC (300°C)	Yb-S	3.5	3.50(12)	0.037(19)
$Yb_2(SO_4)_3 \cdot 8H_2O$ (RT)*	Yb-O	8	2.24 – 2.44	N/A
$Yb_2(SO_4)_3 \cdot 8H_2O$ (RT)*	Yb-S	4	3.60	N/A

* Diffraction data of crystal solid from X-ray diffraction by L Hiltunen et al. (Hiltunen and Niinisto, 1976)

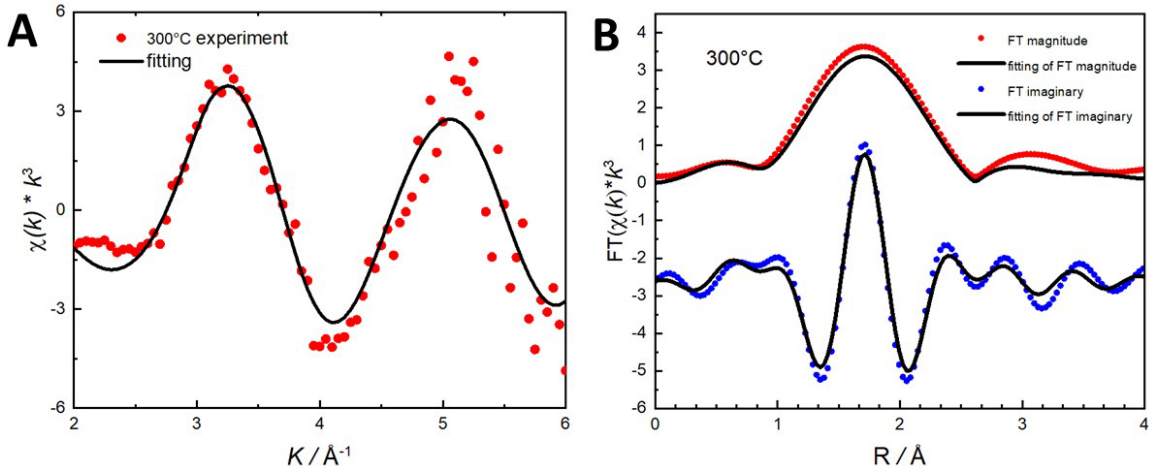

Figure 4. (A) Yb L-III edge EXAFS (red points) and the curvefit (line) for 0.05M $Yb_2(SO_4)_3$ at 300 °C, shown in k^3 weighted k-space. (B) Yb L-III edge EXAFS (red points for the Fourier-transformed magnitude, and blue points for the Fourier-transformed imaginary components) and the curvefit (line) for 0.05M $Yb_2(SO_4)_3$ at 300 °C, shown in k^3 weighted *R*-space and not phase-corrected.

3.3. Local atomic structure and coordination dynamics of Yb^{3+} from AIMD

At RT, the coordination environment of Yb^{3+} is defined by a dense hydration shell and strong sulfate binding. The radial distribution function (RDF) for Yb–O (**Figure 5A**) shows distinct peaks corresponding to five water molecules and three sulfate oxygen atoms, resulting in a total

coordination number (CN) of ~7.95 (**Figure 5B**). The Yb–O bond lengths vary with CN, while mono-dentate sulfate oxygen forming the shortest bond (~2.38 Å) and bi-dentate sulfate oxygen and water oxygen exhibit longer distances (as shown the broader peaks at ~2.65 Å and ~3.03 Å in **Figure 5A**). Analysis of the AIMD trajectories revealed that the RDF feature near ~3.03 Å arises primarily from the distal oxygen in bi-dentate sulfate ligands. In such configurations, one sulfate oxygen binds strongly to Yb^{3+} at a short distance (~2.3–2.5 Å), while the second, more weakly interacting oxygen, lies farther away (~3.0–3.3 Å), contributing to the longer-range RDF peak. These two asymmetric binding modes yield a distorted square antiprism geometry due to the uneven Coulombic repulsion between ligands and angular strain from bi-dentate sulfate ligands (as illustrated in **Figure 6A-B**). Although the beading strain for the molecular structures could destabilize the complex, the presence of π-bonding signature could compensate for these distortions. As shown in molecular orbital visualizations in **Figure 6C-D**, the electron density is always in a shoulder-to-shoulder shape, which suggests a synergistic overlap of ligand-based π orbitals with Yb, which could introduce extra covalency to the bonding and stabilize the molecule to exist in geometrically distorted forms without significant energetic penalties.

As the temperature increases to 100°C, the Yb–O RDF peaks broaden slightly, with minor elongation in bond lengths (sharp peak at ~2.39 Å for mono-dentate sulfate oxygen and broad peaks at ~2.67 Å and ~3.03 Å for bi-dentate sulfate and water oxygens, as in **Figure 5B**). Despite these changes, the CN remains stable at ~7.90 (**Figure 5H**), indicating that the hydration shell is still intact at this temperature. The coordination geometry remains distorted, as the bi-dentate sulfate binding mode persists. The Yb–S RDF (**Figure 5E**) at 100°C shows that mono-dentate sulfate coordination (3.04 Å) becomes more prominent, while bi-dentate sulfate coordination exhibits a slight shift (~3.37 Å), suggesting increased thermal motion and dynamic exchange

between sulfate and water ligands. Significant structural reorganization occurs at 200°C due to dehydration and increased thermal effects. The Yb–O CN decreases to ~7.19 (**Figure 5I**) and exhibits a capped octahedron geometry (**Figure 6E-F**), reflecting the loss of one water molecule from the hydration shell. The Yb–O RDF (**Figure 5C**) shows broader and more variable bond lengths (ranging from 2.26 Å to 3.13 Å), indicative of greater structural disorder. However, the Yb–S RDF (**Figure 5F**) demonstrates a pronounced peak at ~3.38 Å for bi-dentate sulfate coordination, suggesting stronger and more rigid sulfate binding. The decrease in Yb–S CN to ~1.54 (**Figure 5L**) highlights the reduced number of sulfate ligands directly coordinating with Yb^{3+}, yet less loss than the dehydration loss.

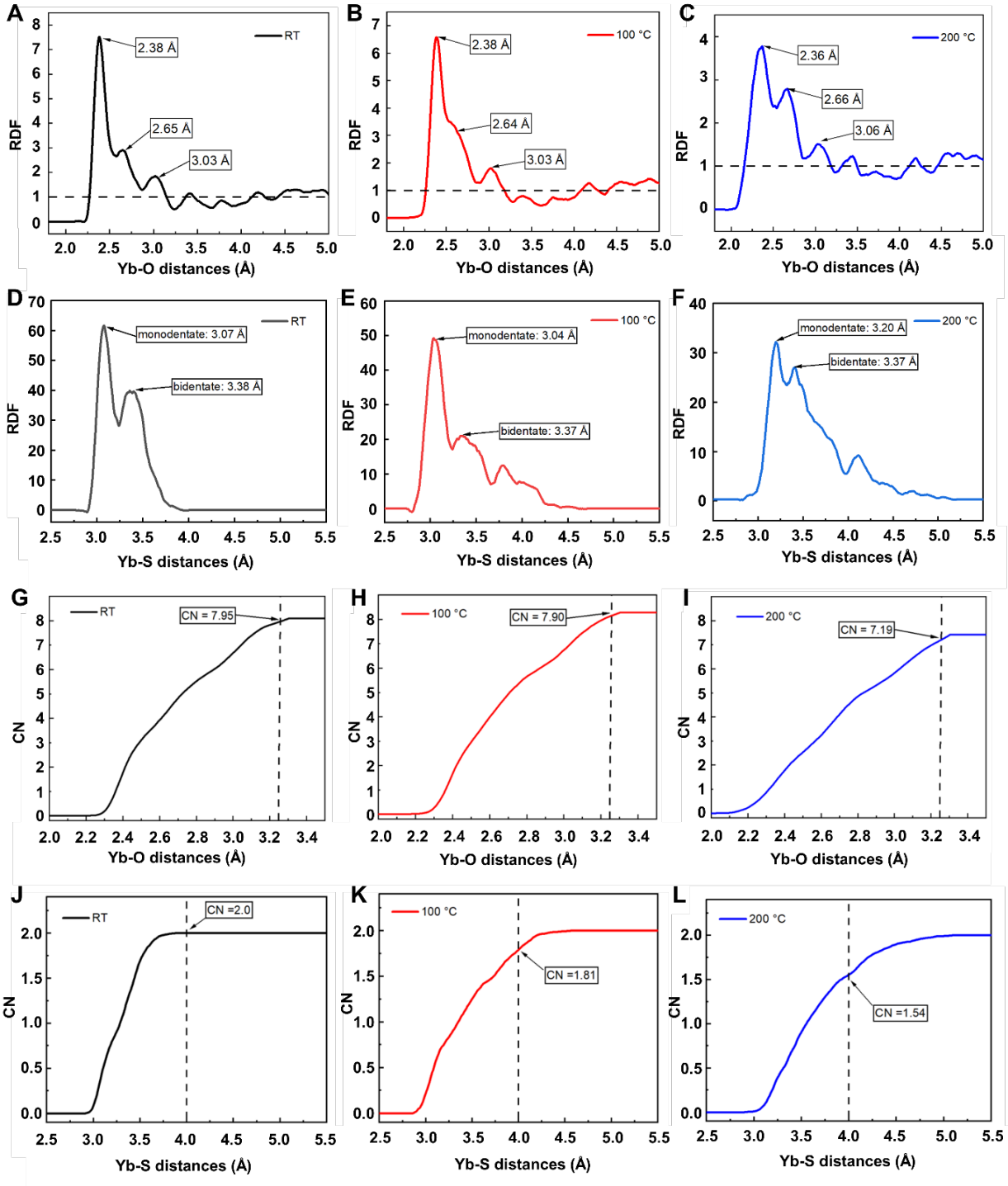

Figure 5. Illustration of the RDF (A--F) and total CN (G--L) for Yb-SO_4 at different temperatures: RT, 100 °C and 200 °C. In the Yb-S RDF illustration, the "monodentate" peak represents the SO_4^{2-} ligand who binds with Yb^{3+} via the monodentate mode, and the "bidentate" peak represents the SO_4^{2-} ligand who binds with Yb^{3+} via the bidentate mode. The Yb-S distance from the monodentate mode is always shorter than the Yb-S distance in the bidentate mode.

406

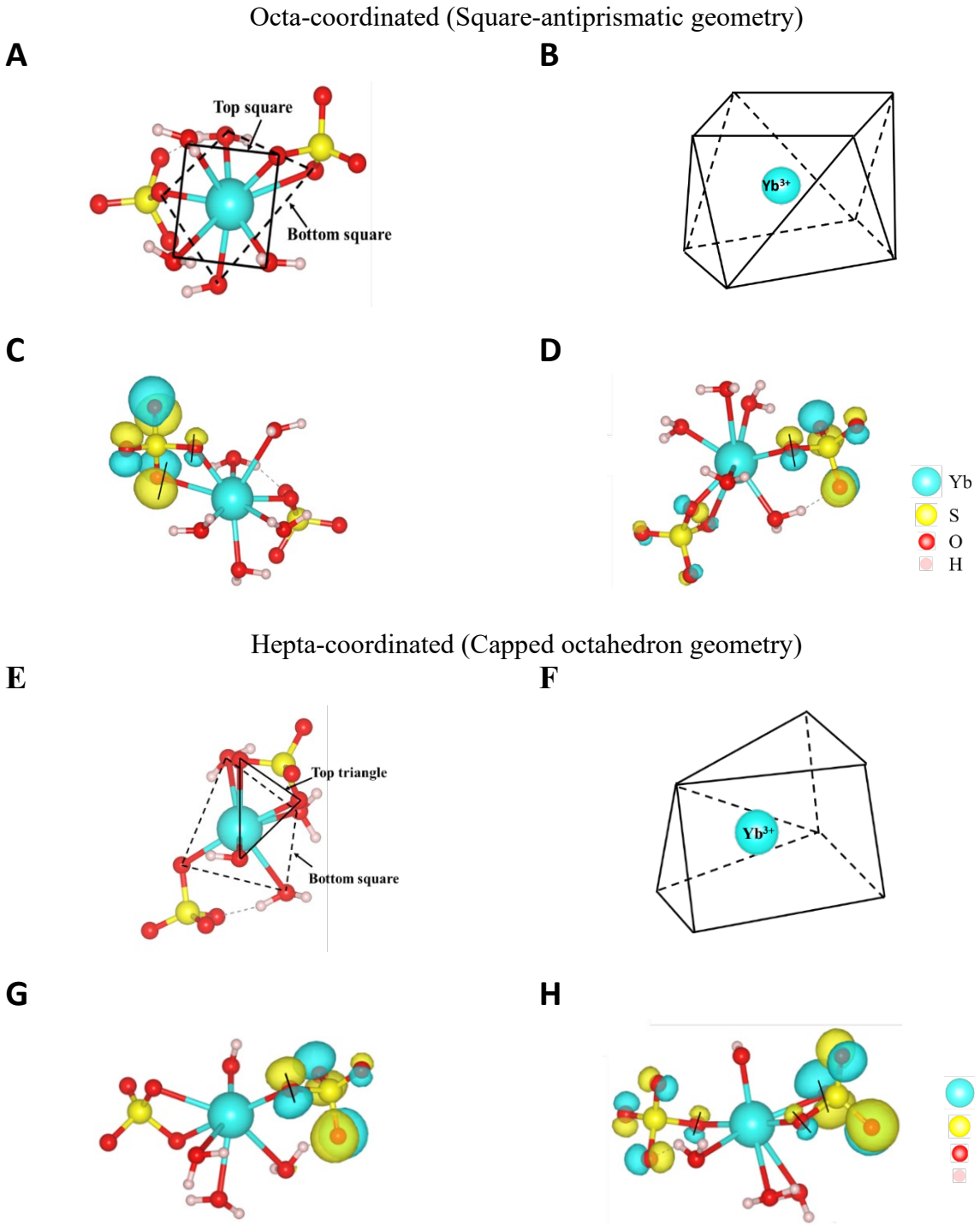

Figure 6. Display of octa- and hepta-coordinated Yb(III)-SO_4 complex from AIMD simulation. The snapshots are respectively from simulations at RT (octa-coordinated) and 200 °C. (A) Molecular structure of the octa-coordinated Yb complex with a square-antiprismatic geometry. (B) Polyhedral representation of the square-antiprismatic coordination geometry of Yb, showing the eight coordinating atoms forming two parallel squares. (C) Electron density visualization of a bonding orbital for the octa-coordinated Yb complex. (D) Electron density visualization of

another bonding orbital for the octa-coordinated Yb complex. (E) Molecular structure of the hepta-coordinated Yb complex with a capped octahedron geometry. (F) Polyhedral representation of the capped octahedron coordination geometry of Yb. (G) Electron density visualization of a bonding orbital for the hepta-coordinated Yb complex. (H) Electron density visualization of another bonding orbital for the hepta-coordinated Yb complex. Cyan atoms represent Yb, yellow atoms represent S, red atoms represent O, and pale pink atoms represent H.

4. Discussion

4.1 Geometry evolution of Yb^{3+} sulfate complexes

The structural dynamics of Yb^{3+}-sulfate complexes show significant temperature-dependent evolution. At RT, Yb^{3+} is coordinated by five water molecules and two sulfate ligands, resulting in a total CN of ~8.5. The coordination geometry corresponds to a distorted square antiprism, with one sulfate ligand binding in a bidentate mode and the other in a monodentate mode. This configuration produces a range of Yb–O bond lengths, with monodentate sulfate bonds at shorter distances (~2.36 Å) and bidentate bonds at longer distances (2.33–3.06 Å). The low Debye-Waller factors (σ^2) for Yb–O and Yb–S bonds indicate minimal thermal disorder, reflecting a stable and ordered coordination environment. These results are consistent across experimental and simulated datasets, underscoring the accuracy of AIMD-derived structural models. At 100°C, the coordination shell of Yb^{3+} remains largely intact. Experimental data suggests slight elongation in Yb–O (~2.35 Å) and Yb–S (~3.68 Å) bond lengths, while the CN stable at ~8.5. However, the increase in σ^2 values for both Yb–O and Yb–S shells suggest enhanced thermal motion and dynamic ligand exchange. AIMD simulations further illustrate this dynamic behavior, showing increased flexibility in sulfate ligands and greater interaction with water molecules. Despite these fluctuations, the overall geometry remains stable, preserving the distorted square antiprism structure.

At 200°C, significant structural reorganization occurs due to thermal effects and partial dehydration. The experimental CN for Yb–O decreases to ~7.8, indicating the displacement of one water molecule from the hydration shell. AIMD simulations confirm this dehydration process and show that the remaining sulfate ligands bind more rigidly to Yb^{3+}. The Yb–S bond length remains stable (~3.64 Å), while the σ^2 for the sulfate shell decreases, suggesting reduced thermal motion and stronger interactions. This transition marks a shift from hydration-dominated coordination to sulfate-dominated coordination, driven by the chelating effect of bidentate sulfate ligands and reduced competition from water molecules.

At 300°C, the coordination environment evolves toward a structure resembling crystalline $Yb_2(SO_4)_3 \cdot 8H_2O$. Experimental EXAFS data show reduced Yb–O coordination (CN ~7.2) and increased Yb–S coordination (CN ~3.5), with shorter Yb–S bond lengths (~3.50 Å). These observations suggest a further decrease in hydration and a dominance of sulfate ligands in the coordination shell. This transition aligns with the retrograde solubility behavior of REE sulfates and hints at the onset of solid-phase formation.

4.2 Geological implications and geological modeling

The coordination environment of Yb^{3+} observed in this study transitions from a hydration-dominated structure at RT to a sulfate-dominated structure at elevated temperatures, contrasting with previous studies on chloride (Cl^-) and fluoride (F^-) complexes. Chloride ligands exhibit weak electrostatic interactions with REEs, leading to more flexible ligand exchange and dynamic hydration shells. This results in a predominantly hydration-controlled transport mechanism, enabling REEs to remain mobile across a broad range of hydrothermal conditions (Mayanovic et al., 2007; Guan et al., 2020). In contrast, fluoride forms strongly bound inner-sphere complexes that restrict REE mobility and promote selective precipitation at relatively lower

449 temperatures(Migdisov and Williams-Jones, 2008). Sulfate ligands, however, exhibit a dual
450 behavior depending on temperature. At RT and 100°C, EXAFS and AIMD results confirm that
451 sulfate coordinates with Yb^{3+} in either a bidentate or monodentate mode, forming stable Yb^{3+}-SO_4
452 complexes in solution. At 200°C, the presence of two mono-dentate sulfate coordination observed
453 suggests that sulfate strengthens its bond with Yb^{3+} as the hydration shell diminishes—unlike
454 chloride complexes, which tend to weaken at high temperatures. Above 200°C, sulfate may start
455 to act as a deposition ligand, given that at 300°C the EXAFS data and AIMD simulations reveal a
456 shift toward sulfate-dominated coordination, resembling the solid-phase $Yb_2(SO_4)_3 \cdot 8H_2O$
457 observed in diffraction studies (Hiltunen and Niinistö, 1976). The reduction in Yb-O coordination
458 number (CN ~7.2) and increased Yb-S interaction (CN ~3.5) indicates the collapse of the hydration
459 shell, favoring sulfate coordination over water. This suggests that sulfate facilitates REE
460 precipitation under high-temperature conditions, consistent with the retrograde solubility of REE
461 sulfates reported in natural hydrothermal deposits (Wan et al., 2023).

462 Unlike Cl^-, which remains a transport ligand across a wider P-T range, sulfate transitions from
463 a stabilizing ligand in solution to a precipitating agent at high temperatures. This temperature-
464 dependent transformation actively regulates REE solubility in hydrothermal fluids, ultimately
465 influencing mineral deposition. The progressive dehydration observed from 100°C to 300°C
466 enhances sulfate complexation strength, reducing REE solubility and triggering precipitation at
467 higher temperatures. Geological evidence indicates that many REE deposits, such as Wicheeda
468 (Canada) and Dalucao (China), formed due to abrupt T-P drops in sulfate-rich fluids (Trofanenko
469 et al., 2016; Zhang et al., 2022). Fluid immiscibility further enhances REE concentration by
470 partitioning REEs into sulfate-rich dense phases, a phenomenon observed in high-grade bastnäsite
471 and monazite deposits (Wan et al., 2021). The increased rigidity of sulfate-bound REEs at high

472 temperatures, as suggested by lower Debye-Waller factors (σ^2) in EXAFS fits, indicates that sulfate
473 complexes play a stabilizing role at moderate temperatures but promote crystallization at higher
474 temperatures. Overall, this temperature-dependent hydration-to-sulfate transition demonstrates
475 that, in the absence of perturbations from other ions, sulfate can function both as a transport agent
476 at lower temperatures and as a deposition trigger at higher temperatures—behavior distinct from
477 chloride or fluoride systems.

478 The molecular-level insights gained from this study also have significant implications for
479 geochemical modeling of REE behavior in hydrothermal systems. Accurate structural data on
480 REE-sulfate complexes at high temperatures and pressures are essential for developing robust
481 thermodynamic models that can predict REE speciation, solubility, and transport in natural
482 hydrothermal fluids. These models are critical for understanding the formation of REE deposits
483 and for guiding exploration and resource assessment strategies. For example, the retrograde
484 solubility behavior of REE sulfates, as observed in this study, can be incorporated into
485 thermodynamic databases to improve the accuracy of predictive models for REE transport and
486 deposition.

487 The temperature-dependent transition from hydration-dominated to sulfate-dominated
488 coordination provides a mechanistic basis for understanding the precipitation of REE-rich minerals
489 in hydrothermal systems. At lower temperatures, sulfate ligands stabilize REEs in solution,
490 facilitating their transport through hydrothermal fluids. However, as temperatures rise, the
491 dehydration of REE complexes and the strengthening of sulfate binding led to the formation of
492 more ordered, sulfate-rich solids. This transition is particularly relevant in high-temperature
493 hydrothermal environments, where sulfate ligands can act as both transport and deposition agents.
494 By integrating these insights into geochemical models, we can better predict the conditions under

495 which REEs are likely to be transported or deposited, aiding in the identification of potential REE
496 resources. While the present study focuses on the bulk fluid conditions, which are representative
497 of hydrothermal veins in natural geological systems. We also recommend further investigation into
498 exploring the behavior of hydrothermal microfluid or fluid under nano confinements. Such
499 conditions are relevant to understanding fluid–rock interactions within mineral nanopores,
500 interlayer spaces of clay minerals, or other restricted geometries commonly found in subsurface
501 environments. Microfluidic and nanoconfinement coupled spectroscopic experiments could
502 complexation, nucleation, and mineral transformation processes of hydrothermal fluids under
503 confinement.

504 Moreover, the structural and stoichiometric information obtained in this study enables the very
505 first and most essential input required to build up reliable geological and thermodynamic models.
506 Accurate coordination environment and stoichiometry of REE–ligand complexes govern how
507 REEs behave in hydrothermal systems, including their solubility, mobility, and eventual
508 deposition. In particular, the long-standing ambiguity over whether Yb in sulfate-rich fluids forms
509 predominantly mono-sulfate ($YbSO_4^+$) or di-sulfate ($Yb(SO_4)_2^-$) complexes has limited the
510 precision of thermodynamic databases. Our AIMD simulations resolve this puzzle by showing that
511 Yb favors the formation of a stable di-sulfate complex up to at least 200 °C, supporting the
512 dominance of the following reaction:

513 $$REE^{3+} + 2SO_4^{2-} \rightleftharpoons REE(SO_4)_2^- \qquad (2)$$

514 while reactions (1) and (3), involving mono-sulfate species, appear to be less relevant under these
515 conditions. At temperatures above 200 °C, complex destabilization and dehydration was evidenced,
516 ultimately leading to precipitation, consistent with REE mineralization. These results not only
517 clarify a long-standing question regarding Yb speciation in sulfate-bearing fluids but also provide

518 robust molecular-level constraints for thermodynamic models, which can be applied to natural
519 systems, such as carbonatite-related REE deposits or hydrothermal veins, to better understand the
520 processes controlling REE enrichment and mineralization. Additionally, the role of fluid
521 immiscibility in concentrating REEs into sulfate-rich dense liquid phases can be incorporated into
522 models to explain the formation of high-grade REE deposits, such as bastnäsite and monazite.

523 The integration of molecular-level insights into geochemical models also has practical
524 applications in resource exploration. By understanding the thermal conditions under which REE
525 sulfates are stable or prone to precipitation, exploration efforts can be targeted toward areas with
526 specific temperature, pressure, and fluid chemistry conditions that favor REE enrichment.
527 Furthermore, the molecular information can inform strategies for the sustainable extraction and
528 recovery of REEs from hydrothermal ore deposits, contributing to the development of more
529 efficient and environmentally friendly mining practices.

530 In conclusion, the molecular-level understanding of Yb^{3+}-sulfate complexes provided by this
531 study offers valuable insights for geochemical modeling of REE behavior in hydrothermal systems.
532 By incorporating these findings into thermodynamic models, we can improve our ability to predict
533 REE transport and deposition, ultimately enhancing our understanding of REE ore formation and
534 guiding the exploration and exploitation of these critical resources.

535 ## 5. Summary

536 This study provides a detailed molecular-level understanding of Yb^{3+} coordination in sulfate-rich
537 hydrothermal fluids under high-pressure and high-temperature conditions. By integrating in situ
538 EXAFS spectroscopy with AIMD simulations, we have characterized the structural evolution of
539 Yb^{3+} complexes in hydrothermal fluid up to 300°C. The results indicate a temperature-dependent

transition in the Yb coordination environment, with hydration shell depletion and increasing sulfate interaction playing key roles in structural reorganization. At room temperature, Yb^{3+} is coordinated by five water molecules and two sulfate ligands, forming a distorted square antiprism geometry with a coordination number of ~8. As the temperature rises, progressive dehydration occurs, reducing water coordination and strengthening sulfate binding. By 200°C, Yb^{3+} adopts a capped octahedron shape with a coordination number of ~7, and sulfate ligands become the dominant coordinating species. At 300°C, further dehydration and precipitation formed due to retrograde solubility of $Yb_2(SO_4)_3$, which also enhanced sulfate binding. These findings have significant geological implications in understanding REE transport and deposition in hydrothermal environments, which reveals sulfate acts as a critical ligand in REE mobility, stabilizing Yb^{3+} in solution at lower temperatures while facilitating precipitation at higher temperatures due to stronger sulfate interactions. The transition from hydration-dominated to sulfate-dominated coordination provides new insights into the mechanisms driving REE mineralization, which could aid in refining predictive geochemical models for REE ore formation under extreme conditions.

CRediT authorship contribution statement

Xiaodong Zhao: Experimental data curation, Calculation, Formal analysis, Investigation, Methodology, Writing – original draft, Writing – review & editing. **Duo Song**: Calculation, Methodology, Resources, Writing – review & editing. **Sebastian Mergelsberg:** Formal analysis, Investigation, Methodology, Writing – review & editing. **Micah Prange**: Formal analysis, Investigation, Methodology, Writing – review & editing. **Daria Boglaienko:** Experimental data curation, Methodology, Writing – review & editing. **Zihua Zhu**: Formal analysis, Writing – review & editing. **Zheming Wang**: Formal analysis, Writing – review & editing. **Carolyn I Pearce**: Methodology, Resources, Supervision, Writing – review & editing. **Chengjun Sun**:

Methodology, Resources, Writing – review & editing. **Kevin M. Rosso**: Writing – review & editing, Supervision, Resources, Funding acquisition. **Xiaofeng Guo**: Conceptualization, Data curation, Formal analysis, Investigation, Methodology, Funding acquisition, Writing – review & editing. **Xin Zhang:** Conceptualization, Investigation, Methodology, Funding acquisition, Writing – review & editing.

Declaration of competing interest

The authors declare that they have no known competing financial interests or personal relationships that could have appeared to influence the work reported in this paper.

Data availability

Data is made available through Mendeley at https://doi.org/10.17632/8sfrxcdmcw.1

Acknowledgements

This work was supported by the U.S. Department of Energy (DOE), Office of Science, Basic Energy Sciences, Chemical Sciences, Geosciences, and Biosciences Division through its Geosciences Program at Pacific Northwest National Laboratory (PNNL) (FWP #56674). XZ and XZ also acknowledge the support from the Laboratory Directed Research and Development (LDRD) program at PNNL, under the Non-Equilibrium Transport Driven Separations Initiative (NETS) and the Advanced Research Projects Agency-Energy's (ARPA-E) Mining Innovations for Negative Emissions Resource Recovery (MINER) program with award number 22CJ0000901, "Re-Mining Red Mud Waste for CO_2 Capture and Storage and Critical Element Recovery (RMCCS-CER)". CIP acknowledge support from IDREAM (Interfacial Dynamics in Radioactive Environments and Materials), an Energy Frontier Research Center funded by the U.S. Department

of Energy (DOE), Office of Science, Basic Energy Sciences (FWP 68932). X.G. acknowledges the support of this work by the National Science Foundation (NSF), Division of Earth Sciences, under award No. 2149848. Part of the research was performed with a user proposal #61223 (Award DOI: 10.46936/lsr.proj.2024.61223/60012698) and 51922 (Award DOI: 10.46936/lser.proj.2021.51922/60000373) at the William R. Wiley Environmental Molecular Sciences Laboratory (EMSL), a national scientific user facility sponsored by the U.S. DOE's Office of Biological and Environmental Research and located at PNNL in Richland, WA. Simulations were performed using the National Energy Research Scientific Computing Center (NERSC) supported by the Office of Science of the U.S. DOE operating under Contract No. DE-AC02-05CH11231. PNNL is a multiprogram national laboratory operated by Battelle Memorial Institute under contract no. DE-AC05-76RL01830 for the DOE. This research used resources of the Advanced Photo Source (APS); a US Department of Energy (DOE) Office of Science user facility operated for the DOE Office of Science by Argonne National Laboratory under contract no. DE-AC02-06CH113577.

References:

Anderson, A.J., Jayanetti, S., Mayanovic, R.A., Bassett, W.A. and Chou, I.-M. (2002) X-ray spectroscopic investigations of fluids in the hydrothermal diamond anvil cell: The hydration structure of aqueous La^{3+} up to 300 °C and 1600 bars. American Mineralogist 87, 262-268.

Apra, E., Bylaska, E.J., De Jong, W.A., Govind, N., Kowalski, K., Straatsma, T.P., Valiev, M., van Dam, H.J., Alexeev, Y. and Anchell, J. (2020) NWChem: Past, present, and future. The Journal of chemical physics 152.

Atwood, D.A. (2013) The rare earth elements: fundamentals and applications. John Wiley & Sons.

Balaram, V. (2019) Rare earth elements: A review of applications, occurrence, exploration, analysis, recycling, and environmental impact. Geoscience Frontiers 10, 1285-1303.

608 Bassett, W.A., Shen, A., Bucknum, M. and Chou, I.-M. (1994) Hydrothermal studies in a new
609 diamond anvil cell up to 10 GPa and from− 190 °C to 1200 °C. Experimental Techniques in
610 Mineral and Rock Physics: The Schreiber Volume, 487-495.

611 Becke, A.D. (2014) Perspective: Fifty years of density-functional theory in chemical physics. The
612 Journal of chemical physics 140.

613 Blöchl, P.E. and Parrinello, M. (1992) Adiabaticity in first-principles molecular dynamics.
614 Physical Review B 45, 9413.

615 Bylaska, E., Tsemekhman, K., Govind, N. and Valiev, M. (2011) Large-scale plane-wave-based
616 density functional theory: formalism, parallelization, and applications. Computational methods for
617 large systems: electronic structure approaches for biotechnology and nanotechnology, 77-116.

618 Car, R. and Parrinello, M. (1985) Unified approach for molecular dynamics and density-functional
619 theory. Physical review letters 55, 2471.

620 Cetiner, Z.S., Wood, S.A. and Gammons, C.H. (2005) The aqueous geochemistry of the rare earth
621 elements. Part XIV. The solubility of rare earth element phosphates from 23 to 150 C. Chemical
622 Geology 217, 147-169.

623 Chen, P., Ilton, E.S., Wang, Z., Rosso, K.M. and Zhang, X. (2024) Global rare earth element
624 resources: A concise review. Applied Geochemistry 175, 106158.

625 Cui, H., Zhong, R., Xie, Y., Yuan, X., Liu, W., Brugger, J. and Yu, C. (2020) Forming sulfate-and
626 REE-rich fluids in the presence of quartz. Geology 48, 145-148.

627 Driesner, T. (2007) The system H_2O–NaCl. Part II: Correlations for molar volume, enthalpy, and
628 isobaric heat capacity from 0 to 1000 ºC, 1 to 5000 bar, and 0 to 1 XNaCl. Geochimica et
629 Cosmochimica Acta 71, 4902-4919.

630 Driesner, T. and Heinrich, C.A. (2007) The system H_2O–NaCl. Part I: Correlation formulae for
631 phase relations in temperature–pressure–composition space from 0 to 1000 ºC, 0 to 5000 bar, and
632 0 to 1 XNaCl. Geochimica et Cosmochimica Acta 71, 4880-4901.

633 Fan, H.-R., Yang, K.-F., Hu, F.-F., Liu, S. and Wang, K.-Y. (2016) The giant Bayan Obo REE-Nb-
634 Fe deposit, China: controversy and ore genesis. Geoscience Frontiers 7, 335-344.

635 Freund, J., Ingalls, R. and Crozier, E. (1989) Extended x-ray-absorption fine-structure study of
636 copper under high pressure. Physical Review B 39, 12537.

637 Girard, P., Namy, J. and Kagan, H. (1980) Divalent lanthanide derivatives in organic synthesis. 1.
638 Mild preparation of samarium iodide and ytterbium iodide and their use as reducing or coupling
639 agents. Journal of the American Chemical Society 102, 2693-2698.

640 Grimme, S., Ehrlich, S. and Goerigk, L. (2011) Effect of the damping function in dispersion
641 corrected density functional theory. Journal of computational chemistry 32, 1456-1465.

642 Guan, Q., Mei, Y., Etschmann, B., Louvel, M., Testemale, D., Spezia, R. and Brugger, J. (2022a)
643 Speciation and thermodynamic properties of La (III)-Cl complexes in hydrothermal fluids: A
644 combined molecular dynamics and in situ X-ray absorption spectroscopy study. Geochimica et
645 Cosmochimica Acta 330, 27-46.

646 Guan, Q., Mei, Y., Etschmann, B., Louvel, M., Testemale, D., Spezia, R. and Brugger, J.J.G.e.C.A.
647 (2022b) Speciation and thermodynamic properties of La (III)-Cl complexes in hydrothermal fluids:
648 A combined molecular dynamics and in situ X-ray absorption spectroscopy study. 330, 27-46.

649 Guan, Q., Mei, Y., Etschmann, B., Testemale, D., Louvel, M. and Brugger, J. (2020) Yttrium
650 complexation and hydration in chloride-rich hydrothermal fluids: a combined ab initio molecular
651 dynamics and in situ X-ray absorption spectroscopy study. Geochimica et Cosmochimica Acta 281,
652 168-189.

653 Hamann, D.R. (1989) Generalized norm-conserving pseudopotentials. Physical Review B 40,
654 2980.

655 Harlov, D.E., Meighan, C.J., Kerr, I.D. and Samson, I.M. (2016) Mineralogy, chemistry, and fluid-
656 aided evolution of the Pea Ridge Fe oxide-(Y+ REE) deposit, southeast Missouri, USA. Economic
657 Geology 111, 1963-1984.

658 Hiltunen, L. and Niinisto, L. (1976) YTTERBIUM SULFATE OCTAHYDRATE, YB2 (SO4) 3.8
659 H2O.

660 Hoover, W.G. (1985) Canonical dynamics: Equilibrium phase-space distributions. Physical review
661 A 31, 1695.

662 Hu, Z., Bertram, S. and Kaindl, G. (1994) X-ray-absorption study of PrO_2 at high pressure.
663 Physical Review B 49, 39.

664 Humphrey, W., Dalke, A. and Schulten, K. (1996) VMD: visual molecular dynamics. Journal of
665 molecular graphics 14, 33-38.

666 Ingalls, R., Crozier, E., Whitmore, J., Seary, A. and Tranquada, J. (1980a) Extended x-ray
667 absorption fine structure of NaBr and Ge at high pressure. Journal of Applied Physics 51, 3158-
668 3163.

669 Ingalls, R., Crozier, E., Whitmore, J., Seary, A. and Tranquada, J.J.J.o.A.P. (1980b) Extended x-
670 ray absorption fine structure of NaBr and Ge at high pressure. 51, 3158-3163.

671 Judge, W., Ng, K., Moldoveanu, G., Kolliopoulos, G., Papangelakis, V. and Azimi, G. (2023)
672 Solubilities of heavy rare earth sulfates in water (gadolinium to lutetium) and H_2SO_4 solutions
673 (dysprosium). Hydrometallurgy 218, 106054.

674 Kaindl, G., Schmiester, G., Sampathkumaran, E. and Wachter, P. (1988) Pressure-induced changes
675 in L III x-ray-absorption near-edge structure of CeO_2 and CeF_4: Relevance to 4 f-electronic
676 structure. Physical Review B 38, 10174.

677 Katayama, Y., Mezouar, M., Itié, J., Besson, J., Syfosse, G., Le Fevre, P. and Di Cicco, A. (1997)
678 High-pressure high-temperature XAFS investigation on HgTe. Le Journal de Physique IV 7, C2-
679 1011-C1012-1012.

680 Kerisit, S., Bylaska, E.J., Massey, M.S., McBriarty, M.E. and Ilton, E.S.J.I.c. (2016) Ab initio
681 molecular dynamics of uranium incorporated in goethite (α-FeOOH): Interpretation of X-ray
682 absorption spectroscopy of trace polyvalent metals. 55, 11736-11746.

683 Kerisit, S.N. and Prange, M.P. (2019) Ab initio molecular dynamics simulation of divalent metal
684 cation incorporation in calcite: implications for interpreting X-ray absorption spectroscopy data.
685 ACS Earth and Space Chemistry 3, 2582-2592.

686 Kerisit, S.N., Prange, M.P.J.A.E. and Chemistry, S. (2019) Ab initio molecular dynamics
687 simulation of divalent metal cation incorporation in calcite: implications for interpreting X-ray
688 absorption spectroscopy data. 3, 2582-2592.

689 Kerisit, S.N. and Prange, M.P.J.C.G. (2020) Ab initio molecular dynamics simulation of Nd3+
690 incorporation in calcite. 534, 119460.

691 Kim, S.Y., Kaup, K., Park, K.-H., Assoud, A., Zhou, L., Liu, J., Wu, X. and Nazar, L.F. (2021)
692 Lithium ytterbium-based halide solid electrolytes for high voltage all-solid-state batteries. ACS
693 Materials Letters 3, 930-938.

694 Kleinman, L. and Bylander, D. (1982) Efficacious form for model pseudopotentials. Physical
695 Review Letters 48, 1425.

696 Lai, X. and Yang, X. (2013) Geochemical characteristics of the Bayan Obo giant REE–Nb–Fe
697 deposit: constraints on its genesis. Journal of South American Earth Sciences 41, 99-112.

698 Latta, D.E., Mergelsberg, S.T., Song, D., Bylaska, E.J., Scherer, M.M., Popejoy, B., Saslow, S.A.,
699 Catalano, J.G., Ilton, E.S.J.E.s. and technology (2025) Effect of Impurities on the Redox Properties
700 of Goethite.

701 Liu, W., Etschmann, B., Mei, Y., Guan, Q., Testemale, D. and Brugger, J. (2020) The role of sulfur
702 in molybdenum transport in hydrothermal fluids: Insight from in situ synchrotron XAS
703 experiments and molecular dynamics simulations. Geochimica et Cosmochimica Acta 290, 162-
704 179.

705 Louvel, M., Etschmann, B., Guan, Q., Testemale, D. and Brugger, J. (2022a) Carbonate
706 complexation enhances hydrothermal transport of rare earth elements in alkaline fluids. Nature
707 Communications 13, 1456.

708 Louvel, M., Etschmann, B., Guan, Q., Testemale, D. and Brugger, J.J.N.C. (2022b) Carbonate
709 complexation enhances hydrothermal transport of rare earth elements in alkaline fluids. 13, 1456.

710 Martínez, L., Andrade, R., Birgin, E.G. and Martínez, J.M. (2009) PACKMOL: A package for
711 building initial configurations for molecular dynamics simulations. Journal of computational
712 chemistry 30, 2157-2164.

713 Mayanovic, R.A., Anderson, A.J., Bassett, W.A. and Chou, I.-M. (2007) On the formation and
714 structure of rare-earth element complexes in aqueous solutions under hydrothermal conditions with
715 new data on gadolinium aqua and chloro complexes. Chemical geology 239, 266-283.

716 Mayanovic, R.A., Anderson, A.J., Bassett, W.A. and Chou, I.-M. (2009a) Steric hindrance and the
717 enhanced stability of light rare-earth elements in hydrothermal fluids. American Mineralogist 94,
718 1487-1490.

719 Mayanovic, R.A., Anderson, A.J., Bassett, W.A. and Chou, I.-M. (2009b) The structure and
720 stability of aqueous rare-earth elements in hydrothermal fluids: new results on neodymium (III)
721 aqua and chloroaqua complexes in aqueous solutions to 500 C and 520 MPa. Chemical Geology
722 259, 30-38.

723 Mayanovic, R.A., Jayanetti, S., Anderson, A.J., Bassett, W.A. and Chou, I.-M. (2002) The structure
724 of Yb^{3+} aquo ion and chloro complexes in aqueous solutions at up to 500 ^{o}C and 270 MPa. The
725 Journal of Physical Chemistry A 106, 6591-6599.

726 Mayanovic, R.A., Jayanetti, S., Anderson, A.J., Bassett, W.A. and Chou, I.-M. (2003) Relaxation
727 of the structure of simple metal ion complexes in aqueous solutions at up to supercritical conditions.
728 The Journal of chemical physics 118, 719-727.

729 McBriarty, M.E., Kerisit, S., Bylaska, E.J., Shaw, S., Morris, K., Ilton, E.S.J.E.s. and technology
730 (2018) Iron vacancies accommodate uranyl incorporation into hematite. 52, 6282-6290.

731 Metz, M.C., Brookins, D.G., Rosenberg, P. and Zartman, R. (1985) Geology and geochemistry of
732 the Snowbird deposit, Mineral County, Montana. Economic Geology 80, 394-409.

733 Migdisov, A., Guo, X., Nisbet, H., Xu, H. and Williams-Jones, A.E. (2019) Fractionation of REE,
734 U, and Th in natural ore-forming hydrothermal systems: Thermodynamic modeling. The Journal
735 of Chemical Thermodynamics 128, 305-319.

736 Migdisov, A., Williams-Jones, A., Brugger, J. and Caporuscio, F.A. (2016) Hydrothermal transport,
737 deposition, and fractionation of the REE: Experimental data and thermodynamic calculations.
738 Chemical Geology 439, 13-42.

739 Migdisov, A.A., Reukov, V. and Williams-Jones, A. (2006) A spectrophotometric study of
740 neodymium (III) complexation in sulfate solutions at elevated temperatures. Geochimica et
741 Cosmochimica Acta 70, 983-992.

742 Migdisov, A.A. and Williams-Jones, A. (2008) A spectrophotometric study of Nd (III), Sm (III)
743 and Er (III) complexation in sulfate-bearing solutions at elevated temperatures. Geochimica et
744 Cosmochimica Acta 72, 5291-5303.

Nosé, S. (1984) A unified formulation of the constant temperature molecular dynamics methods. The Journal of chemical physics 81, 511-519.

Obšil, M., Majer, V., Hefter, G.T. and Hynek, V. (1997) Densities and apparent molar volumes of Na_2SO_4 (aq) and K_2SO_4 (aq) at temperatures from 298 K to 573 K and at pressures up to 30 MPa. Journal of Chemical & Engineering Data 42, 137-142.

Ohsumi, K., Sueno, S., Nakai, I., Imafuku, M., Morikawa, H., Kimata, M., Nomura, M. and Shimomura, O. (1986) EXAFS measurement under high pressure by diamond anvil cell. Le Journal de Physique Colloques 47, C8-189-C188-192.

Pask, H., Carman, R.J., Hanna, D.C., Tropper, A.C., Mackechnie, C.J., Barber, P.R. and Dawes, J.M. (1995) Ytterbium-doped silica fiber lasers: versatile sources for the 1-1.2/spl mu/m region. IEEE Journal of Selected Topics in Quantum Electronics 1, 2-13.

Perdew, J.P., Burke, K. and Ernzerhof, M. (1996) Generalized gradient approximation made simple. Physical review letters 77, 3865.

Prange, M.P., Mergelsberg, S.T. and Kerisit, S.N. (2021) Ab initio molecular dynamics simulations of amorphous calcium carbonate: Interpretation of pair distribution function and X-ray absorption spectroscopy data. Crystal Growth & Design 21, 2212-2221.

Ravel, B. and Newville, M. (2005) ATHENA, ARTEMIS, HEPHAESTUS: data analysis for X-ray absorption spectroscopy using IFEFFIT. Journal of synchrotron radiation 12, 537-541.

Seidler, G., Mortensen, D., Remesnik, A., Pacold, J., Ball, N., Barry, N., Styczinski, M. and Hoidn, O. (2014) A laboratory-based hard x-ray monochromator for high-resolution x-ray emission spectroscopy and x-ray absorption near edge structure measurements. Review of scientific instruments 85.

Smith, M., Henderson, P. and Campbell, L. (2000) Fractionation of the REE during hydrothermal processes: constraints from the Bayan Obo Fe-REE-Nb deposit, Inner Mongolia, China. Geochimica et Cosmochimica Acta 64, 3141-3160.

Sueno, S., Nakai, I., Imafuku, M., Morikawa, H., Kimata, M., Ohsumi, K., Nomura, M. and Shimomura, O. (1986) EXAFS Measurements under high pressure conditions using a combination of a diamond anvil cell and synchrotron radiation. Chemistry Letters 15, 1663-1666.

Takasu, Y., Komori, K., Honda, K., Kumakura, M., Yabuzaki, T. and Takahashi, Y. (2004) Photoassociation spectroscopy of laser-cooled ytterbium atoms. Physical review letters 93, 123202.

Trofanenko, J., Williams-Jones, A., Simandl, G. and Migdisov, A. (2016) The nature and origin of the REE mineralization in the Wicheeda Carbonatite, British Columbia, Canada. Economic Geology 111, 199-223.

Troullier, N. and Martins, J.L. (1991) Efficient pseudopotentials for plane-wave calculations. Physical review B 43, 1993.

Valiev, M., Bylaska, E.J., Govind, N., Kowalski, K., Straatsma, T.P., Van Dam, H.J.J., Wang, D., Nieplocha, J., Aprà, E. and Windus, T.L. (2010) NWChem: A comprehensive and scalable open-source solution for large scale molecular simulations. Computer Physics Communications 181, 1477-1489.

Verlet, L.J.P.r. (1967) Computer" experiments" on classical fluids. I. Thermodynamical properties of Lennard-Jones molecules. 159, 98.

Verplanck, P.L., Mariano, A.N. and Mariano, A. (2016) Rare earth element ore geology of carbonatites.

Wan, Y., Chou, I.-M., Wang, X., Wang, R. and Li, X. (2023) Hydrothermal sulfate surges promote rare earth element transport and mineralization. Geology 51, 449-453.

Wan, Y., Wang, X., Chou, I.-M. and Li, X. (2021) Role of sulfate in the transport and enrichment of REE in hydrothermal systems. Earth and Planetary Science Letters 569, 117068.

Williams-Jones, A.E., Samson, I.M. and Olivo, G.R. (2000) The genesis of hydrothermal fluorite-REE deposits in the Gallinas Mountains, New Mexico. Economic Geology 95, 327-341.

Xu, Y., Zhao, X., Hua, W., Wang, W., Zhao, M., Xiao, W., Hou, X., Guo, X., Pan, D., Wu, W.J.S. and Technology, P. (2024) Spatially confined coordination platform in covalent organic framework for selective uranium adsorption from aqueous solutions. 345, 127307.

Zhang, W., Chen, W.T., Mernagh, T.P. and Zhou, L. (2022) Quantifying the nature of ore-forming fluids in the Dalucao carbonatite-related REE deposit, Southwest China: implication for the transport and deposition of REEs. Mineralium Deposita, 1-19.

800 Zhao, X., Guillen, T.R., Graham, T.R., Chen, P., Zhao, Y., Mergelsberg, S.T., Zhu, Z., Wang, Z.,
801 Rosso, K.M. and Guo, X. (2024) Incorporation of rare earth elements Sc, Y and La into gibbsite.
802 Chemical Engineering Journal 485, 149809.

803 Zheng, X. and Liu, Y. (2019) Mechanisms of element precipitation in carbonatite-related rare-earth
804 element deposits: Evidence from fluid inclusions in the Maoniuping deposit, Sichuan Province,
805 southwestern China. Ore Geology Reviews 107, 218-238.

806